

PAPER • OPEN ACCESS

An experimental and theoretical study of the Kr 3d correlation satellites

To cite this article: M D Kiselev *et al* 2022 *J. Phys. B: At. Mol. Opt. Phys.* **55** 055002

View the [article online](#) for updates and enhancements.

You may also like

- [An optimal transport approach for seismic tomography: application to 3D full waveform inversion](#)
L Métivier, R Brossier, Q Mérigot *et al.*
- [The Kr valence photoelectron satellite lines in the photon energy region below the 3d threshold](#)
A Caló, S Atanassova, R Sankari *et al.*
- [Time-and-energy-resolved measurement of Auger cascades following Kr 3d excitation by attosecond pulses](#)
A J Verhoef, A V Mitrofanov, X T Nguyen *et al.*



IOP | ebooks™

Bringing together innovative digital publishing with leading authors from the global scientific community.

Start exploring the collection—download the first chapter of every title for free.

An experimental and theoretical study of the Kr 3d correlation satellites

M D Kiselev^{1,2,3} , M Reinhardt⁴ , M Patanen⁴ , A Kivimäki^{4,5} , I Powis⁶ , O Zatsarinny⁷, A N Grum-Grzhimailo²  and D M P Holland^{8,*} 

¹ Faculty of Physics, Lomonosov Moscow State University, Moscow 119991, Russia

² Skobeltsyn Institute of Nuclear Physics, Lomonosov Moscow State University, Moscow 119991, Russia

³ Laboratory for Modeling of Quantum Processes, Pacific National University, 680035 Khabarovsk, Russia

⁴ Nano and Molecular Systems Research Unit, Faculty of Science, University of Oulu, PO Box 3000, 90014 Oulu, Finland

⁵ MAX IV Laboratory, Lund University, PO Box 118, 22100 Lund, Sweden

⁶ School of Chemistry, The University of Nottingham, University Park, Nottingham, NG7 2RD, United Kingdom

⁷ Department of Physics and Astronomy, Drake University, Des Moines, IA 50311, United States of America

⁸ Daresbury Laboratory, Daresbury, Warrington, Cheshire WA4 4AD, United Kingdom

E-mail: md.kiselev@physics.msu.ru and david.holland@stfc.ac.uk

Received 15 November 2021, revised 27 January 2022

Accepted for publication 4 February 2022

Published 4 April 2022



CrossMark

Abstract

The Kr 3d correlation satellites have been studied experimentally by using plane polarized synchrotron radiation to record polarization dependent photoelectron spectra (PES), and theoretically by employing the R-matrix method to calculate photoionization cross sections, PES and angular distributions. The experimental spectra have allowed the photoelectron anisotropy parameters characterizing the angular distributions, and the intensity branching ratios, related to the photoionization partial cross sections, to be evaluated. The results are discussed in terms of normal and conjugate shake-up processes. The experimental and calculated photoelectron angular distributions associated with those correlation satellites that arise predominantly through conjugate shake-up mechanisms are shown to be isotropic. In contrast, the anisotropy parameters associated with satellites due to normal shake-up processes exhibit a dependence on electron kinetic energy similar to that of the anisotropy parameters corresponding to the Kr 3d main lines. The theoretical results include an analysis of the partial waves representing the emitted photoelectron and, for certain correlation satellites, show that a particular ionization continuum dominates. This, in turn, may allow the dominant normal or conjugate shake-up mechanism forming the satellite to be identified.

Keywords: krypton photoelectron spectrum, photoionization cross section, correlation satellites, shake-up formation, R-matrix calculations

(Some figures may appear in colour only in the online journal)

* Author to whom any correspondence should be addressed.



Original content from this work may be used under the terms of the [Creative Commons Attribution 4.0 licence](https://creativecommons.org/licenses/by/4.0/). Any further distribution of this work must maintain attribution to the author(s) and the title of the work, journal citation and DOI.

1. Introduction

The photoelectron spectrum due to ionization of a particular atomic level often exhibits weak satellite structure at binding energies (BE) higher than that of the prominent main line associated with the single-hole state. Early experimental studies on the inert gases employed conventional, fixed photon energy, x-ray sources, and several comprehensive reviews of this work are available [1–5]. Historically, the satellite structure was usually discussed in relation to the shake model [6–8], involving the simultaneous ionization of one electron and the excitation of another. Subsequent investigations using plane polarized synchrotron radiation enabled the photon energy dependence of the satellite formation to be studied, whilst also allowing the angular distribution of the electrons associated with the satellites to be measured. The aim was to investigate whether this additional energy dependent information could help elucidate the satellite formation mechanisms [9–12].

The satellites observed in the experimental spectra arise from electron correlation, and nowadays are more generally referred to as correlation satellites [10]. Within a configuration interaction (CI) description, the effects of electron correlation may be separated into two parts: configuration interaction in the initial state (ISCI) and configuration interaction in the final state (FSCI) [4, 8, 10]. The latter interaction may be subdivided into final ionic state CI (FISCI) and continuum state CI (CSCI). ISCI and FISCI refer to electron systems comprising N and $N - 1$ electrons, respectively. In CSCI, the continuum photoelectron is included, and hence is an N -particle CI.

In the theoretical description of the processes leading to satellite formation, two types of electron correlation are often distinguished [9, 13]: (i) intrinsic correlation effects which are due to the interaction between the passive electrons and the core hole vacancy, and are nearly independent of the photon energy; and (ii) dynamic correlation effects which depend upon the photoionization dynamics and should manifest themselves most prominently near threshold.

ISCI and FISCI are, to a first approximation, independent of the photoelectron kinetic energy, and are hence considered as intrinsic correlations. Satellites deriving their intensity from intrinsic correlations should display a constant branching ratio with respect to the main photoelectron line. Moreover, the angular distribution of the electrons associated with the satellites arising from intrinsic correlations should be similar to those in the main line [10].

In contrast, dynamic correlations depend upon the interactions between the departing photoelectron, as it leaves the surrounding environment, and the passive electrons. The shake model [6–8], which takes into account the interaction between the passive electrons and the hole created by the photoionization process leads, in the sudden limit [10, 14] where the passive electrons have insufficient time to relax into their final state, to an energy independent branching ratio between the shake-up satellites and the main line. However, for low electron kinetic energies, the core electrons have sufficient time to adjust adiabatically to a certain extent to the changing environment [15], and the resulting relaxation leads to an energy

dependence, with the shake-up satellite intensity decreasing towards the ionization threshold [9, 13].

CSCI incorporates the interaction between continuum states, where these states describe the entire photoionization channel comprising the final ionic state and the photoelectron. CSCI gives rise to the so-called conjugate shake-up satellites [16]. Using the terminology associated with the shake model, a normal shake-up process involves the dipole ionization of one electron together with the monopole excitation of a second electron, whereas a conjugate shake-up process is due to the monopole ionization of one electron accompanied by the dipole excitation of a second. Thus, in a normal process the angular momentum of the photon is transferred to the photoelectron and the symmetry of the outgoing wave representing the departing electron is changed by an odd number, most likely by 1 ($\Delta l = \pm 1$) [13]. In a conjugate process the angular momentum remains in the ion and the symmetry of the outgoing photoelectron wave is preserved ($\Delta l = 0$) [13]. Under these conditions, the photoelectron angular distribution (PAD) for ionization of an unpolarized atom becomes isotropic [17–19]. The relative intensity of the conjugate shake-up peaks is predicted to increase towards the ionization threshold [9, 13].

Most of the experiments employing synchrotron radiation to record correlation satellite structure in the inert gases have concentrated on the outer valence orbitals (see, e.g. [11, 12, 20–28]). Very little work has been carried out on the Kr 3d satellites which are the focus of the present study. The first experimental studies [5, 29] providing reasonable quality spectra encompassing the Kr 3d correlation structure were carried out with Mg and Al $K\alpha$ photon sources. Later work [30], performed with synchrotron radiation, enabled the photoionization partial cross sections and the PADs for the Kr 3d main lines and satellites to be measured. However, in that study, the experimental resolution was insufficient to allow individual satellite peaks to be resolved. A higher resolution spectrum of the satellites, assigned using Hartree–Fock (HF) energy calculations and intensity estimations based on the sudden approximation, was obtained by Sankari *et al* [31], but the PADs could not be measured. Hayaishi *et al* [32] measured the threshold photoelectron spectrum in the Kr 3d shake-up region and proposed assignments, based on the results obtained from multiconfigurational Dirac–Fock calculations, for some of the observed structure. The peaks were discussed in relation to normal and conjugate shake-up processes. Bolognesi *et al* [33] have measured threshold photoelectron coincidence spectra and threshold photoelectron spectra in the energy range 105–127 eV, and observed the $\text{Kr}^{2+} 3d^{-1}4p^{-1}$ doubly charged ion states and the $\text{Kr}^+ 3d^{-1}4p^{-1}nl$ satellite states.

The normal ($SU1$ – $SU4$) and conjugate ($SU5$ – $SU8$) shake-up processes relevant to our study of the Kr 3d correlation satellites are given in table 1. It is interesting to note from examination of this table that the $3d^{-1}4s^{-1}np$, nf and $3d^{-1}4p^{-1}nf$ ionic configurations can only be formed through the conjugate shake-up mechanism whilst the $3d^{-1}4s^{-1}ns$, nd configurations can only be formed through the normal shake-up mechanism. In contrast, the $3d^{-1}4p^{-1}np$, nd configurations may be produced via either a normal or a conjugate

Table 1. Shake-up mechanisms relevant to the formation of the Kr 3d correlation satellites.

Shake process	Ionization	Excitation	Ionic configuration
Normal shake-up			
SU1	3d → εp, εf	4p → np	3d ⁻¹ 4p ⁻¹ np
SU2	3d → εp, εf	4s → ns	3d ⁻¹ 4s ⁻¹ ns
SU3	4p → εs, εd	3d → nd	3d ⁻¹ 4p ⁻¹ nd
SU4	4s → εp	3d → nd	3d ⁻¹ 4s ⁻¹ nd
Conjugate shake-up			
SU5	3d → εd	4p → ns, nd	3d ⁻¹ 4p ⁻¹ ns, nd
SU6	3d → εd	4s → np	3d ⁻¹ 4s ⁻¹ np
SU7	4p → εp	3d → np, nf	3d ⁻¹ 4p ⁻¹ np, nf
SU8	4s → εs	3d → np, nf	3d ⁻¹ 4s ⁻¹ np, nf

mechanism. As will be shown, in some cases our calculated l -dependent photoionization partial cross sections enable the more likely shake-up mechanism to be identified where more than one formation process is allowed. Additional information may be provided by the value of the photoelectron anisotropy parameter.

In the present work, plane polarized synchrotron radiation was employed to measure polarization dependent PES encompassing the Kr 3d correlation satellites. These allowed the PAD, as characterized by the anisotropy parameter β , and the intensity branching ratio (proportional to the photoionization partial cross section) of a specific satellite to be evaluated. The selected binding energy range allowed satellites due to the 3d⁻¹4p⁻¹nl and 3d⁻¹4s⁻¹nl configurations to be studied. The R-matrix approach was used to calculate the photoionization amplitudes for the various satellite states, thereby enabling the structure observed in the experimental spectrum to be assigned. In addition, the photoelectron anisotropy parameter associated with a specific satellite state was calculated as a function of photon energy.

The paper is organized as follows. In section 2 we describe the experiment. In section 3 the theoretical model is presented. Section 4 contains our results together with their discussion, followed by a short summary.

2. Experimental apparatus and procedure

The experiment was performed at the newly commissioned FinEstBeAMS beamline on the 1.5 GeV storage ring at the MAXIV Laboratory in Lund, Sweden. Detailed descriptions of the beamline [34, 35], the gas phase end station [36], and the experimental procedure [37] have already been reported. Hence, only a brief summary of the pertinent details is given here.

The beamline uses an in-house designed undulator, based on the APPLE-II design [38]. The beamline control system allows the undulator gap and the polarization of the synchrotron radiation to be selected, enabling the use of plane and circularly polarized radiation.

A toroidal mirror collimates the beam emitted by the undulator prior to the radiation entering a plane grating monochromator [39]. A 600 lines/mm grating was used in the present

work. A further toroidal mirror focusses the monochromatic radiation onto the monochromator exit slit, after which an ellipsoidal mirror refocusses the radiation into the experimental chamber. An SXUV100 photodiode, mounted at the exit of the chamber, could be used to measure the photon flux.

The PES were recorded at the gas phase end-station using the Scienta R4000 hemispherical electron analyser. The analyser was mounted in a fixed position such that the entrance lens of the analyser lies parallel to the plane of the electron orbit in the storage ring. The analyser pass energy was set to 10 eV, which, when combined with the 0.8 mm curved entrance slit width, results in a theoretical resolution of 20 meV.

The BE of the Kr 3d correlation satellites studied in the present work ranged from 110 to 130 eV, and PES were recorded at several photon energies between 127.5 and 200 eV. For the satellite with the binding energy of 110 eV, the translational Doppler broadening [40] varied between ~6 and 13 meV at photon energies of 127.5 and 200 eV, respectively. A monochromator exit slit width of 200 μm was used, resulting in the theoretical optical resolution varying between 88 meV ($h\nu = 127.5$ eV) and 173 meV ($h\nu = 200$ eV), for all measurements except that at 133 eV, where an exit slit width of 100 μm was used, resulting in a resolution of 47 meV. Thus, the overall resolution, due to the contributions from the translational Doppler broadening, the electron analyser and the photon bandwidth, varied from 51 meV at a photon energy of 133 eV to 175 meV at a photon energy of 200 eV.

The Kr gas, with a stated purity of 99.998%, was ordered from AGA Gas AG (Linde). It was introduced into the chamber via a needle, with an internal diameter of 0.1 mm, mounted on a port aligner.

The differential photoionization ionic state resolved cross section, $d\sigma/d\Omega$, varies as a function of the angle θ between the polarization vector of the incoming plane polarized radiation and the velocity vector of the outgoing photoelectron. Within the electric dipole approximation and assuming perfectly polarized radiation, the dependency is given by [41]

$$\frac{d\sigma}{d\Omega} = \frac{\sigma}{4\pi} [1 + \beta P_2(\cos \theta)], \quad (1)$$

where σ is the angle-integrated ionic state resolved cross section; $d\Omega$ is the differential solid angle element in the direction specified by the polar angle θ ; β is the photoelectron anisotropy parameter; and $P_2(\cos \theta)$ is the Legendre polynomial of second order. At each photon energy, PES were recorded with the plane of polarization lying either parallel ($\theta = 0^\circ$) or perpendicular ($\theta = 90^\circ$) to the Scienta analyser's electron acceptance axis. Defining I_0 and I_{90} as the normalized electron intensities for parallel and perpendicular polarization orientations, respectively, allows (1) to be rearranged into the form [42, 43]

$$\beta = \frac{2(I_0 - I_{90})}{I_0 + 2I_{90}}. \quad (2)$$

All the spectra were normalized to the sample pressure, the accumulation time, the photon flux, and the electron spectrometer transmission efficiency [37] prior to processing.

Before performing our measurements on the Kr 3d correlation satellites, the performance of the beamline and the

electron spectrometer was checked by recording polarization dependent PES encompassing the $\text{Kr}^+4p^5\ ^2P_{1/2}$ and $\ ^2P_{3/2}$ states, over the photon energy range 110–200 eV, and the $\text{Ar}^+3p^5\ ^2P_{1/2}$ and $\ ^2P_{3/2}$ states, over the range 32–66 eV. The β -parameters derived from these spectra were in accord with the well-established values [30, 44, 45]. Thus, the procedure to change the plane of polarization by shifting the magnet arrays in the undulator [34] appeared reproducible, in terms of photon beam position and energy.

The binding energy scale of the PES of the Kr 3d main lines and correlation satellites was calibrated using the $\text{Kr}^+3d^9\ ^2D_{5/2}$ state ionization energy of 93.81 eV [5].

Previous experimental studies [46–48] have shown that the $M_{45}NN$ and $M_{45}NN-NNN$ Auger transitions in krypton give rise to spectral features in the kinetic energy range $\sim 15-57$ eV. Thus, these Auger peaks overlap those due to the Kr 3d correlation satellites at certain photon energies. An electron spectrum was recorded at a photon energy of 225 eV, where the peaks due to the Auger transitions are well separated from those associated with the correlation satellites. This spectrum was used to assess the contribution from Auger peaks at photon energies where the peaks due to the Auger transitions could overlap those due to the correlation satellites.

The experimental photoelectron anisotropy parameter and the branching ratio associated with a particular satellite state were determined as described by Powis *et al* [42]. For each satellite peak, the electron counts in the normalized parallel polarization spectrum are summed, as are those in the perpendicular polarization spectrum, and the resulting total counts are inserted into (2). The potential errors in the β -parameters and branching ratios were estimated by propagation of the assumed statistical counting uncertainty through evaluation of (2). The resulting error bars do not include any uncertainty associated with possible systematic errors.

3. Theoretical model

We simulate the photoionization of neutral krypton from the ground state,

$$h\nu + \text{Kr}(\alpha_0 J_0^{\pi_0}) \rightarrow \text{Kr}^+(\alpha J^\pi) + e^-(\varepsilon l), \quad (3)$$

in the electric dipole (E1) approximation. Here J_0 and π_0 (J and π) are the total angular momentum and the parity of the ground atomic (final ionic) state, α_0 (α) is a corresponding set of quantities further specifying the state, εl denotes the energy ε and the orbital momentum l of the photoelectron. According to the dipole selection rules, the total angular momentum and parity of the final system ($\text{Kr}^+ + e^-$) are $J_{\text{tot}} = 1$ and $\pi_{\text{tot}} = -1$, respectively. These two quantities are the only strict quantum numbers of the final system, neglecting nuclear degrees of freedom.

In order to calculate the photoionization amplitudes of process (3), we used an R-matrix approach based on a semi-relativistic version of the B-spline R-matrix code [49]. This version partially takes into account the non-orthogonality of the electron orbitals, fully takes into account interchannel

interaction and allows diagonalization of the Breit–Pauli Hamiltonian. The formalism of the R-matrix approach for calculations of the cross sections, and the anisotropy parameters characterizing the PAD, has been published [49] and does not need to be repeated. Therefore we concentrate on specific features of our model used in the calculations for the process (3).

The initial state of atomic krypton, described by the wave function ψ_0 , was obtained by a full self-consistent HF calculation [50] of the $[\text{Ar}] 3d^{10}4s^24p^6$ configuration. The final ionic states (thresholds) are represented by the following mixed set of electronic configurations (above the $[\text{Ar}]$ core):

$$\begin{aligned} &3d^{10}4s^24p^5, \quad 3d^{10}4s^24p^44d, \quad 3d^{10}4s^14p^6, \\ &3d^94s^24p^6, \quad 3d^94s^24p^5np, \quad 3d^94s^24p^5ns, \quad 3d^94s^24p^5md, \\ &3d^94s^14p^6np, \quad 3d^94s^14p^6ns, \quad 3d^94s^14p^6md, \end{aligned}$$

where $n = 5-7$, and $m = 4-5$.

All the configurations in set (4) with a closed 3d-shell have the same core of inner orbitals up to 3d from the independent self-consistent calculation of the $[\text{Ar}] 3d^{10}4s^24p^5$ configuration. States with a 3d-hole from set (4) also have the same core but with inner orbitals up to 3d from the independent self-consistent calculation of the $[\text{Ar}] 3d^94s^24p^6$ configuration.

For the configurational set (4), due to the Breit–Pauli interaction, all possible LS-terms are split in energy for $J = 1/2; 3/2; 5/2$, giving in total 244 LSJ-coupled ionic states (thresholds). In the final ($\text{Kr}^+ + e^-$) system, we use the jK-coupling scheme between the residual ion and the photoelectron [51], where the ionic angular momentum first couples with the orbital momentum of the photoelectron into the intermediate momentum $\mathbf{K} = \mathbf{J}_i + \mathbf{l}$, and then the electron spin is added, resulting in the total angular momentum of the channel $\mathbf{J}_{\text{tot}} = \mathbf{K} + \mathbf{s}$. With the above set of Kr^+ states, this leads to 627 photoionization channels satisfying the dipole selection rules.

The total photoionization cross section for a given photon energy $h\nu$ is a sum over partial (channel) ionization cross sections σ_j

$$\sigma_{\text{tot}}(h\nu) = \sum_{j=1}^{N_{\text{ch}}} \sigma_j(h\nu), \quad (5)$$

where N_{ch} is the number of photoionization channels.

In order to simulate the PES observed in the experiment, we build up the function:

$$f_{\text{PES}}(\varepsilon) = \sum_i P_i(h\nu) \cdot \exp\left[-\frac{(\varepsilon + I_i - h\nu)^2}{\Gamma^2(h\nu)}\right], \quad (6)$$

where $P_i(h\nu) = \frac{\sigma_i(h\nu)}{\sigma_{\text{tot}}(h\nu)}$ is the relative contribution of the ionization of neutral krypton into a particular ionic state i to the total photoionization cross section σ_{tot} at the photon energy $h\nu$, I_i is the ionization energy of the ionic state i relative to the ground state of neutral krypton, $\Gamma(h\nu)$ is the total experimental resolution, as discussed in section 2, for photon energy $h\nu$.

After constructing the function (6), the amplitude of the most intense peak in the theoretical spectrum (labelled peak I,

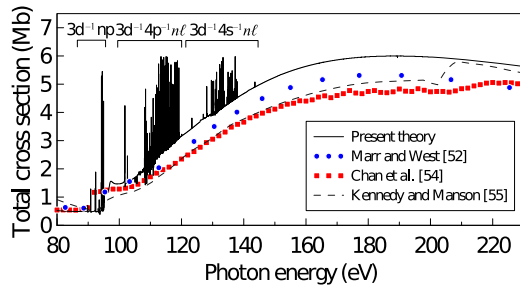


Figure 1. The total photoionization cross section of krypton. Solid black curve—R-matrix calculations from the present work; dashed black curve—theoretical results from [55]; red squares—experimental data from [54]; blue circles - experimental data from [52]. The groups of autoionization series in Kr and Kr^+ are indicated near the top of the figure.

see section 4) is scaled to the height of the corresponding peak in the experimental spectrum. All other peaks in the theoretical spectrum are scaled by the same factor. This process enables the theoretical and experimental spectra to be compared in a simple way.

4. Results and discussion

4.1. Overview

Figure 1 shows the calculated total photoionization cross section of krypton, obtained by summation over all ionization channels, in the photon energy range 80–230 eV. The sharp structure predicted at energies below 100 eV arises from autoionization of the Rydberg series $3d^{-1}np$ ($n = 4, 5, \dots, \infty$), converging to the M_4 and M_5 -shell ionization thresholds, whose experimental energies are 95.05 and 93.81 eV, respectively [5]. For comparison, our HF ionization energies of these two orbitals are 94.71 and 93.42 eV, respectively. Two bands of narrow and intense closely-spaced features at higher energy are due to the $3d^{-1}4p^{-1}nl$ and $3d^{-1}4s^{-1}nl$ shake-up autoionizing states, respectively. The calculated cross section in the regions free of resonances is in good agreement with the experimental measurements [32, 52–54]. The narrowness and high intensity of the resonances are due to the restricted basis set used in the R-matrix calculations. Although the calculations do not include the main decay channels of these resonances, this omission hardly affects the total and partial cross sections in energy regions devoid of resonances.

The difference between the length and velocity gauges in the present calculations is at the average level of 2%–7% (depending on the channel under consideration). As the velocity-form matrix elements depend mainly on the low-radius part of wavefunctions, whereas those of the length-form depend mainly on the large-radius part, and because the considered processes are mainly connected with the outer shells of krypton (3d and higher), we find length-gauge results to be more appropriate and accurate. Therefore, in this paper we present only the results in the length gauge.

The experimental magic angle photoelectron spectrum obtained from the polarization dependent spectra, in the region of $3d^{-1}4p^{-1}nl$ states, recorded at a photon energy of 190 eV

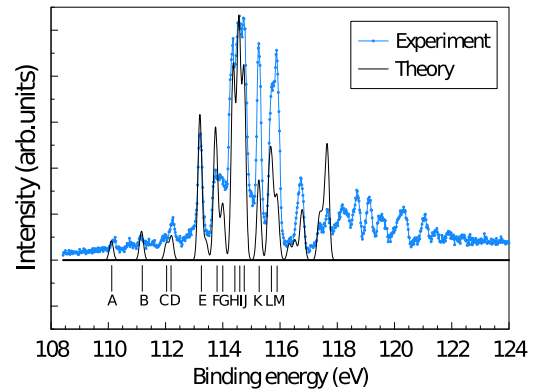


Figure 2. The magic angle photoelectron spectrum obtained from the polarization dependent spectra recorded at a photon energy of 190 eV, together with the simulated spectrum, in the binding energy region corresponding to the $3d^{-1}4p^{-1}nl$ states.

is plotted in figure 2, together with the theoretically simulated spectrum at the same energy. In the latter spectrum, 0.6 eV has been added to the HF BE to improve the agreement between the experimental and the theoretical peak positions. The calculated BE, after adding 0.6 eV, are listed in table 2. The calculated photoelectron spectrum has been convoluted with a function (6) representing the combined experimental electron spectrometer and monochromator resolutions at a particular photon energy. Theoretical spectra were generated in this manner at photon energies of 163, 175, 180, 190 and 200 eV. The relative peak intensities were almost independent of the photon energy, in accord with the experimental results. Therefore the discussion of the spectra will focus on that simulated at 190 eV. Experimental spectra were also recorded at photon energies of 127.5, 133 and 136 eV. However, at these energies the theoretical spectra are strongly affected by autoionization.

According to our theoretical results, the structure observed in the binding energy region ~ 110 – 122 eV is due to the $3d^{-1}4p^{-1}nl$ ($l = s, p, d$) states, while that in the ~ 124 – 132 eV region arises from the $3d^{-1}4s^{-1}nl$ ($l = s, p, d$) states. The latter states will be discussed in section 4.4, but note that the results from our calculations offer a new interpretation for the structure around 126 eV, where they show the importance of the $3d^9 4s^1 4p^6 4d$ and $3d^9 4s^1 4p^6 5p$ configurations, in addition to the $3d^9 4s^1 4p^6 5s$ configuration. The assignments proposed by Sankari *et al* [31] only involved the latter configuration. The identifications of the peaks associated with the $3d^{-1}4p^{-1}nl$ states are given in table 2. For each peak, the leading electron configuration and the term are specified. Our calculations show that the leading configuration associated with peak J, at a binding energy of ~ 114.8 eV, is $3d^9 4s^2 4p^5(^1P)5p[^2D_{3/2}]$, thereby clarifying the earlier assignment of 4d or 5p [32]. Furthermore, the identification of peak M, with a binding energy of ~ 115.90 eV, is $3d^9 4s^2 4p^5(^1P)5p[^2P_{3/2}]$ in contrast to the proposed assignment of 6s or 6p [32].

The binding energy region 118–122 eV encompasses numerous closely spaced and strongly mixed states, namely the $3d^9 4s^2 4p^5 nl$ ($l = d, f; n = 5, 6, \dots$) states. Each of these states contains many LSJ-levels. Owing to computational restrictions, this region is beyond our present analysis.

Table 2. Identification of the photoelectron peaks appearing in the simulated spectra encompassing the $\text{Kr}^+ 3d^9 4s^2 4p^5 nl$ correlation satellites. The leading electron configuration and the term is given for each peak. The first parenthesis indicates the $3d^9 4p$ electronic state, and the term with the total momentum J of the electron configuration is given in square brackets. The calculated BE, after adding 0.6 eV, are listed in the final column.

Peak label	Identification	Leading percentage	Theoretical BE (eV)
A	$3d^9 4s^2 4p^5 ({}^3D) 5s [{}^2D_{3/2}]$	46%	110.13
B	$3d^9 4s^2 4p^5 ({}^3P) 5s [{}^2P_{3/2}]$	64%	111.17
C	$3d^9 4s^2 4p^5 ({}^1P) 5s [{}^2P_{1/2}]$	60%	112.05
D	$3d^9 4s^2 4p^5 ({}^3D) 5p [{}^2D_{5/2}]$	70%	112.22
E	$3d^9 4s^2 4p^5 ({}^3D) 5p [{}^2F_{5/2}]$	58%	113.20
F	$3d^9 4s^2 4p^5 ({}^3P) 5p [{}^2P_{3/2}]$	58%	113.76
G	$3d^9 4s^2 4p^5 ({}^3F) 5p [{}^2F_{5/2}]$	50%	114.01
H	$3d^9 4s^2 4p^5 ({}^3F) 4d [{}^2P_{3/2}]$	26%	114.42
I	$3d^9 4s^2 4p^5 ({}^1F) 5p [{}^2D_{5/2}]$	50%	114.59
J	$3d^9 4s^2 4p^5 ({}^1P) 5p [{}^2D_{3/2}]$	49%	114.75
K	$3d^9 4s^2 4p^5 ({}^1D) 6p [{}^2D_{5/2}]$	62%	115.28
L	$3d^9 4s^2 4p^5 ({}^3D) 6p [{}^2D_{5/2}]$	83%	115.69
M	$3d^9 4s^2 4p^5 ({}^1P) 5p [{}^2P_{3/2}]$	73%	115.90

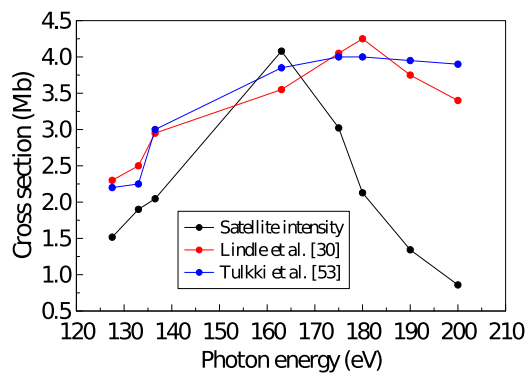


Figure 3. The arbitrarily scaled relative photoionization cross section for the encompassed satellites (see text for details) and the Kr 3d photoionization cross section which we have estimated from the data reported by Tulkki *et al* [53] and Lindle *et al* [30].

At each photon energy used to record spectra in the present study, a relative photoionization cross section for the Kr 3d correlation satellites lying in the binding energy range 113.0–116.1 eV was evaluated by summing the electron counts within this energy range and normalizing to the photodiode current (after taking into account the quantum efficiency). The photoionization cross section for the encompassed satellites, obtained in this manner, is plotted in figure 3, arbitrarily scaled to allow a straight forward comparison with the Kr 3d photoionization cross section which we have estimated from the data reported by Lindle *et al* [30] and Tulkki *et al* [53]. The comparison indicates that the satellite cross section appears to decrease relative to the σ_{3d} photoionization cross section as the photon energy increases.

The ratio of the intensity in the satellites observed between ~ 113 and 117 eV to that in the Kr $3d_{5/2}$, $3d_{3/2}$ main lines was estimated from a spectrum recorded at a photon energy of 225 eV. The resulting value, averaged over all J -components, of 0.16 ± 0.01 is higher than those obtained previously (0.08 ± 0.01 [30] and ~ 0.1 [32]).

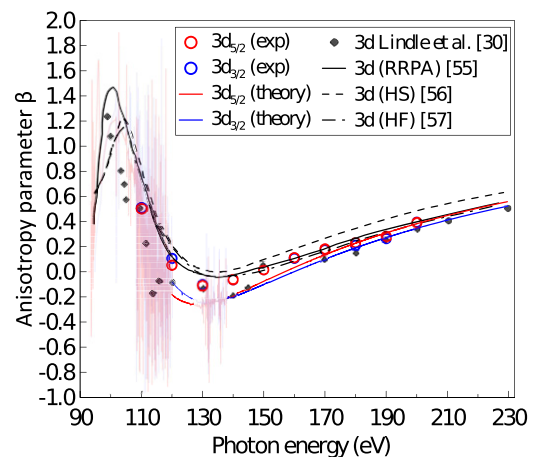


Figure 4. Photoelectron anisotropy parameters for the Kr $3d_{5/2}$ and $3d_{3/2}$ main lines. Solid red and blue curves—R-matrix calculations from the present work for Kr $3d_{5/2}$ and $3d_{3/2}$, respectively. Other curves: relativistic random phase approximation from [56] (solid black curve); Hartree–Slater calculation from [57] (dashed black curve); HF calculation from [55] (dash-dotted black curve). Experimental data: present work (red and blue open circles for Kr $3d_{5/2}$ and $3d_{3/2}$, respectively); from [30] (black diamonds). All the depicted theoretical results are in the length form. For the sake of clarity, the theoretical results in the autoionization regions are plotted more lightly.

Before turning to the satellite lines, we show in figure 4 a compilation of results for the photoelectron β -parameters for the Kr $3d_{5/2}$ and $3d_{3/2}$ main lines, together with our values.

The energy dependence of our spin–orbit split experimental main line β -parameters is similar to that for the unresolved spin–orbit β -parameter reported by Lindle *et al* [30]. Our theoretical β -parameters are in good agreement with both sets of experimental data. In comparison with the previous theoretical results, our calculated curves appear qualitatively closer to the values reported by Lindle *et al* [30], particularly in the region of the minimum around ~ 130 eV. However, the

Table 3. Binding energy ranges (accounting for the experimental peak width) used to analyse the $\text{Kr}^+ 3d^{-1}4p^{-1}nl$ correlation satellites.

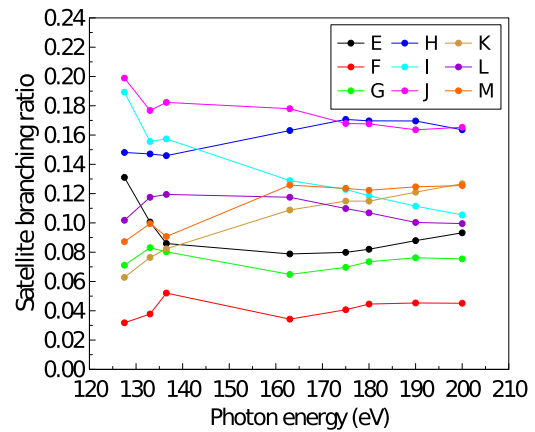
Peak	Binding energy range (eV)
E	113.00–113.42
F	113.56–113.79
G	113.79–114.12
H	114.12–114.48
I	114.48–114.65
J	114.65–115.00
K	115.12–115.42
L	115.52–115.79
M	115.79–116.10

most significant result enabled within the framework of our R-matrix calculations is the demonstration of the energy dependencies of the spin-orbit split β -parameters, corresponding to the $\text{Kr}^+ (3d_{5/2})^{-1}$ and $(3d_{3/2})^{-1}$ ionic states. The differing photon energy dependencies of these calculated β -parameters are consistent with the experimental results. In particular, in the photon energy region below the minimum in the β value, the calculated β -parameter for the $3d_{5/2}$ component is slightly lower than that for the $3d_{3/2}$ component, in accord with experiment, whilst at photon energies above 130 eV, this ordering is reversed ($\beta_{5/2} > \beta_{3/2}$), again consistent with experiment.

4.2. Photoelectron anisotropy parameters and branching ratios for the $3d^{-1}4p^{-1}nl$ correlation satellites

The polarization dependent PES were processed to obtain β -parameters and branching ratios for the most prominent of the $3d^{-1}4p^{-1}nl$ correlation satellites, namely those labelled E–M in figure 2 and table 2. The binding energy ranges used for these satellites are given in table 3. The branching ratio for a specific satellite, at a particular photon energy, is defined as the intensity in that satellite peak divided by the sum of the intensities in all (E–M) the satellites. Thus, at each photon energy, the branching ratios sum to unity. Figure 5 shows that the satellite branching ratios remain approximately constant as a function of photon energy.

We consider first the overall photon energy dependence of the β -parameters associated with satellite peaks E–M, plotted in figure 6. The theoretical results shown in that figure correspond to the unconvoluted data. Thus, for energies below ~ 140 eV the predictions exhibit numerous narrow resonances due to autoionization. In general, the calculated β -parameters are in good agreement with the experimental values. The average binding energy of the satellite peaks E–M (~ 115 eV) is approximately 20 eV higher than that of the main lines. Taking this shift in BE into account, the β -parameters for the main lines and those for the peaks E–M all pass through a minimum at a kinetic energy of ~ 35 – 45 eV. Thus, the anisotropy parameters for the main lines exhibit an energy dependence similar to those associated with the shake-up peaks. Such a dependence is expected of satellites deriving their intensity from intrinsic correlations. Although the β -parameters for peaks E–M exhibit, in general, a similar energy dependence to that of the

**Figure 5.** The experimental satellite branching ratios for the $3d^{-1}4p^{-1}nl$ correlation satellites. Labels in the legend correspond to those indicated in figure 2 and table 2.

main line, the individual β -parameters do display some significant differences and this point will now be discussed in relation to peaks H–M.

In figure 7, the magic angle PES and the anisotropy β -parameters, obtained at photon energies of 127.5, 163 and 190 eV, are plotted as a function of binding energy. These plots illustrate the way in which the β -values depend upon the satellite peak. It is noticeable that for the neighbouring peaks H, I and J, the β -value associated with peak H is always substantially higher than that for peak I. Also, the β -value for peak L differs markedly from that for peak M. According to table 1, peaks I and J could be produced through process $SU1$, which is a normal shake-up process, or through process $SU7$, which is a conjugate shake-up process. As will be shown later in our discussion of the photoionization partial cross sections, peaks I and J arise primarily through a normal shake-up process. In contrast, peak H can arise through a normal shake-up process $SU3$ or a conjugate shake-up process $SU5$. Peaks L and M result, predominantly, from a normal shake-up mechanism, and yet the β -values associated with these two peaks differ significantly.

Although peaks A and B are fairly weak (see figure 2), the polarization dependent spectra (figure 8) show that the intensities in peaks A and B in the $\theta = 0^\circ$ spectrum are approximately the same as those in the corresponding peaks in the $\theta = 90^\circ$ spectrum. Thus, the PAD associated with each of these peaks is roughly isotropic, corresponding to $\beta \sim 0$. As will be discussed, this observation is consistent with our theoretical predictions indicating that peaks A and B arise primarily through a conjugate shake-up process, namely process $SU5$. Peak C, also predicted to be due primarily to a conjugate shake-up process, overlaps to some extent with peak D, arising mainly from a normal shake-up process.

4.3. Shake-up mechanisms for the $\text{Kr}^+ 3d^{-1}4p^{-1}nl$ correlation satellites

To distinguish between normal and conjugate shake-up mechanisms, we need to examine the angular momenta l of the photoelectrons for each mechanism (table 1), and to compare

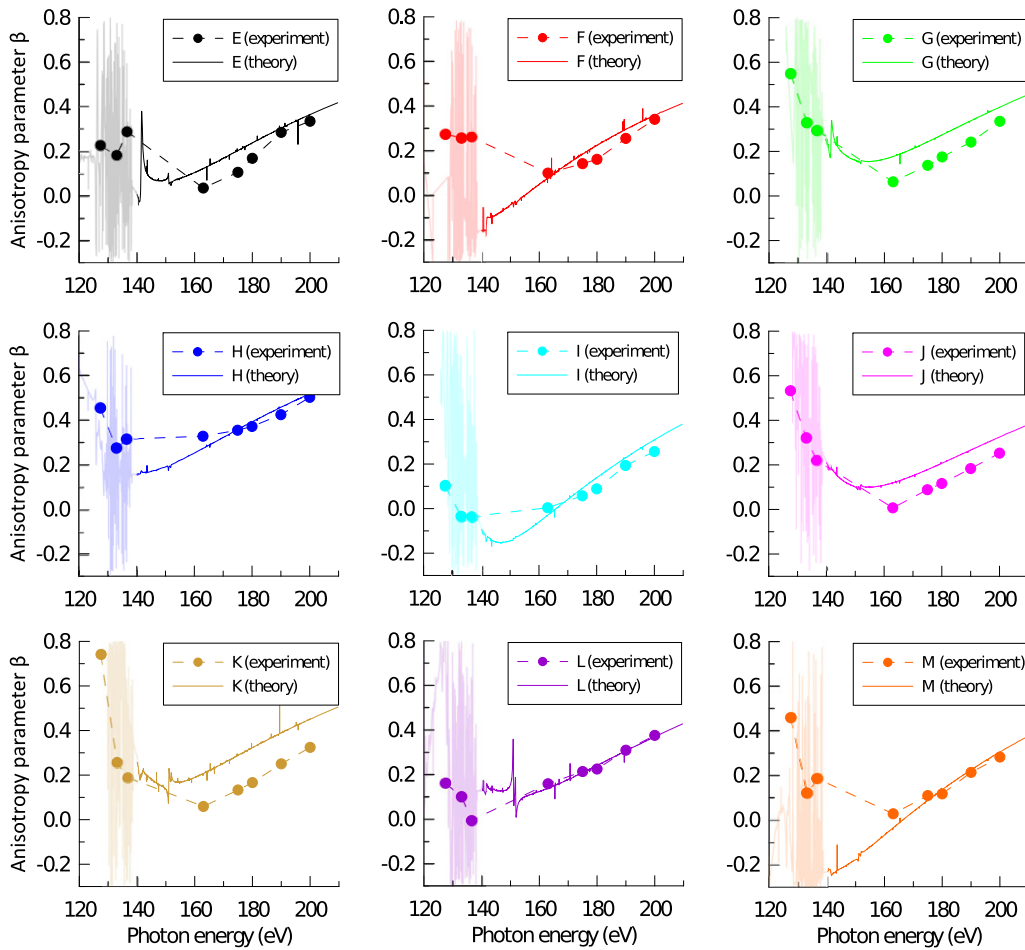


Figure 6. Photoelectron anisotropy parameters associated with the satellite peaks E–M (table 2). For the sake of clarity, the theoretical results in the autoionization regions are plotted more lightly.

these with the calculated contributions for different l (photoionization channels) for a given configuration of the residual ion. These l -dependent contributions can be extracted from our R-matrix calculations, and a comparison between the contributions for a particular ionic configuration may enable the dominant formation mechanism to be identified.

In the present work, the jK-coupling scheme between the photoelectron and the residual ion has been adopted to describe the photoionization process (3):

$$\mathbf{J} + \mathbf{l} = \mathbf{K}$$

$$\mathbf{K} + 1/2 = \mathbf{J}(\text{Kr}^+ + e^-)$$

$$\mathbf{J}(\text{Kr}^+ + e^-) = \mathbf{J}_0 + \mathbf{J}(\gamma) = 0 + 1 = 1$$

and l should also satisfy the parity conservation

$$\text{condition} : \pi_0 \cdot \pi(\gamma) = \pi \cdot (-1)^l.$$

We consider in detail the probable shake-up processes for the correlation satellites. The dominant configuration contributing to peak A is $3d^9 4s^2 4p^5(^3D)5s[{}^2D_{3/2}]$ (table 2). Thus $J(\text{ion}) = 3/2$. As an example, let us derive all the quantum numbers connected with peak A formation. As $\mathbf{K} + 1/2 = \mathbf{1}$

we have two allowed values for K : $1/2$ and $3/2$. After that, the condition $\mathbf{J}(\text{ion}) + \mathbf{l}(\text{electron}) = \mathbf{K}$ leads to two relations: $3/2 + l = 1/2$ and $3/2 + l = 3/2$. These result in $l = 1; 2$ for $K = 1/2$ and $l = 0; 1; 2; 3$ for $K = 3/2$. According to the parity conservation condition, peak A can only be associated with even l -waves. Thus, according to the jK-coupling scheme, we have 3 types of photoelectron waves (which will henceforth be denoted as $\epsilon l [K]$): $\epsilon d [1/2]$; $\epsilon s [3/2]$; $\epsilon d [3/2]$. These three photoionization partial cross sections are plotted in figure 9(a).

At this point, it is important to distinguish between a theoretical model in which a single isolated state, with a certain configuration, is associated with a particular peak, and the model used in our R-matrix calculations. In a non-interacting state model, the dominant $3d^9 4s^2 4p^5(^3D)5s[{}^2D_{3/2}]$ configuration of peak A (table 2) would produce strictly a d-wave in the continuum through the conjugate shake-up mechanism $SU5$. However, our R-matrix calculations are based on a model in which all the states are mixed states. Our results show that the leading configuration for peak A has a leading percentage of 46%, but, in addition to this contribution, other admixtures to this state with significant contributions are:

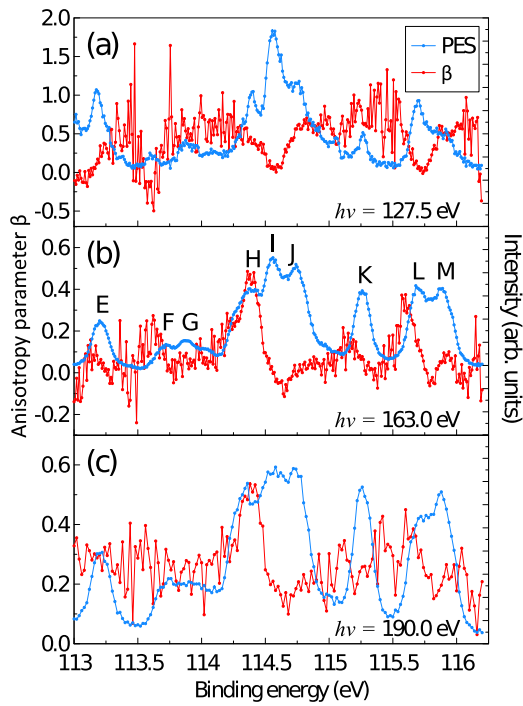


Figure 7. The magic angle PES and the anisotropy β -parameters, obtained at photon energies of 127.5 eV (a), 163 eV (b) and 190 eV (c) as a function of binding energy. Labels of the peaks correspond to those given in table 2. The left hand axis refers to the anisotropy parameters and the right hand axis refers to the photoelectron intensity.

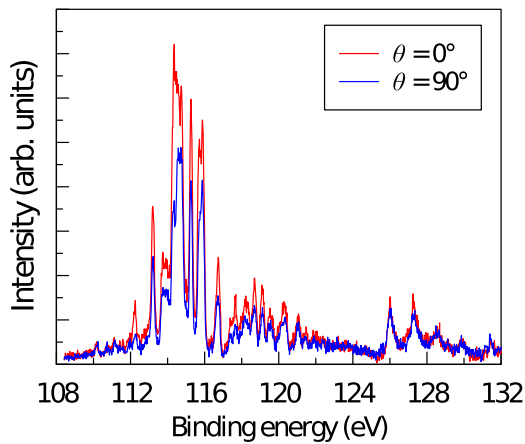


Figure 8. The polarization dependent PES, recorded at $h\nu = 190$ eV, with the plane of polarization lying parallel ($\theta = 0^\circ$) and perpendicular ($\theta = 90^\circ$) to the Scienta analyser's electron acceptance axis.

$$3d^9 4s^2 4p^5(^1D) 4d[{}^2D_{3/2}] \quad 16\%$$

$$3d^9 4s^2 4p^5(^3P) 5s[{}^2P_{3/2}] \quad 11\%$$

$$3d^9 4s^2 4p^5(^1P) 5s[{}^2P_{3/2}] \quad 10\%$$

+ other states with smaller contributions.

Thus, we have a 16% admixture of the $3d^9 4s^2 4p^5(^1D) 4d[{}^2D_{3/2}]$ state to the leading configuration

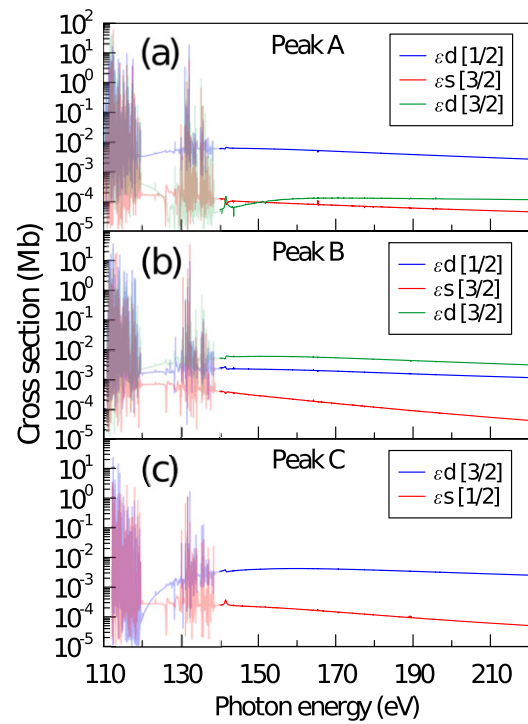


Figure 9. Photoionization partial cross sections for peak A (a), peak B (b) and peak C (c). For the sake of clarity, the theoretical results in the autoionization regions are plotted more lightly.

of peak A, and this electronic state could be produced either by the conjugate shake-up mechanism (again with a d-wave continuum) or by a normal shake-up mechanism (with d- and s-continua). The possibility of the s-wave production by the admixed states explains the presence of the $\epsilon s [3/2]$ contribution in the l -dependent photoionization partial cross sections for peak A. Since the $\epsilon s [3/2]$ contribution is two orders of magnitude smaller than the $\epsilon d [1/2]$ contribution, and the s-wave can be produced only through a normal shake-up mechanism, we can conclude that peak A originates predominantly through a conjugate shake-up process.

Further evidence in support of the formation mechanism for peak A being a conjugate shake-up process, is provided by our calculated β -parameter (figure 10(a)). The theoretical anisotropy parameter for peak A is close to zero at 190 eV, in accord with our experimental result.

For peak B, all the quantum numbers are the same as those for peak A. This allows similar conclusions to be made concerning the formation mechanism and the energy dependence of the anisotropy parameter for peak B. Details of the theoretical results for peak B are presented in figures 9(b) and 10(b).

For peak C ($3d^9 4s^2 4p^5(^1P) 5s[{}^2P_{1/2}]$) we have two types of photoelectron waves: $\epsilon s [1/2]$ and $\epsilon d [3/2]$. Figure 9(c) shows that the d-wave is dominant in the formation of satellite C. Therefore, peak C is formed by a conjugate shake-up mechanism.

For peak D ($3d^9 4s^2 4p^5(^3D) 5p[{}^2D_{5/2}]$) we have three photoelectron waves: $\epsilon f [1/2]$; $\epsilon p [3/2]$ and $\epsilon f [3/2]$. Normal SU1

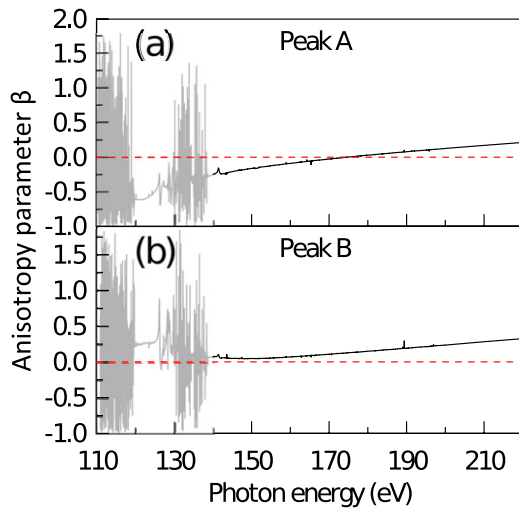


Figure 10. Calculated photoelectron anisotropy parameters for peak A (a) and peak B (b). For the sake of clarity, the theoretical results in the autoionization regions are plotted more lightly. Dashed red line indicates the $\beta = 0$ value.

and conjugate $SU7$ shake-up mechanisms contribute to the formation of peak D, but we can conclude from the shake mechanisms that the f-wave connects only with the normal shake-up process. For the p-waves, the situation is less clear because in the R-matrix method it is only possible to distinguish the different l values of the electrons, and not the mechanism of its production. Thus the cross section contributions for p-waves give information about the cumulative influence of normal and conjugate shake-up mechanisms. However, the l -dependent photoionization cross sections (figure 11(a)), show that the contribution of the f-waves is ~ 10 times higher than that of the p-waves in the photon energy region greater than 140 eV (relevant to our experiment). Therefore, we can conclude that peak D is created predominantly by a normal shake-up mechanism.

For peak E, all the quantum numbers are the same as those for peak D. Thus, the formation mechanism for peak E is a normal shake-up process. Details of the theoretical results for peak E are presented in figure 11(b).

For peak F, the main contribution arises from the configuration $3d^9 4s^2 4p^5 (^3P) 5p [^2P_{3/2}]$ giving us three photoelectron waves: $\epsilon p [1/2]$; $\epsilon p [3/2]$ and $\epsilon f [3/2]$. From the cross section contributions plotted in figure 11(c), we can conclude that peak F is formed predominantly through a normal shake-up mechanism. Interestingly, in the photon energy range 137–143 eV, the contributions of the p- and f-waves are comparable, suggesting that interference effects might be observed between the normal and conjugate shake-up processes.

For peak G, all the quantum numbers are the same as those for peaks D and E. Therefore, peak G is created through a normal shake-up mechanism. Details of the theoretical results for peak G are presented in figure 11(d).

For peak H ($3d^9 4s^2 4p^5 (^3F) 4d [^2P_{3/2}]$) we have three photoelectron waves: $\epsilon d [1/2]$; $\epsilon s [3/2]$ and $\epsilon d [3/2]$. The s-wave connects only with the normal shake-up process $SU3$, but the d-waves result from the cumulative influence of the normal $SU3$ and conjugate $SU5$ shake-up mechanisms. The cross

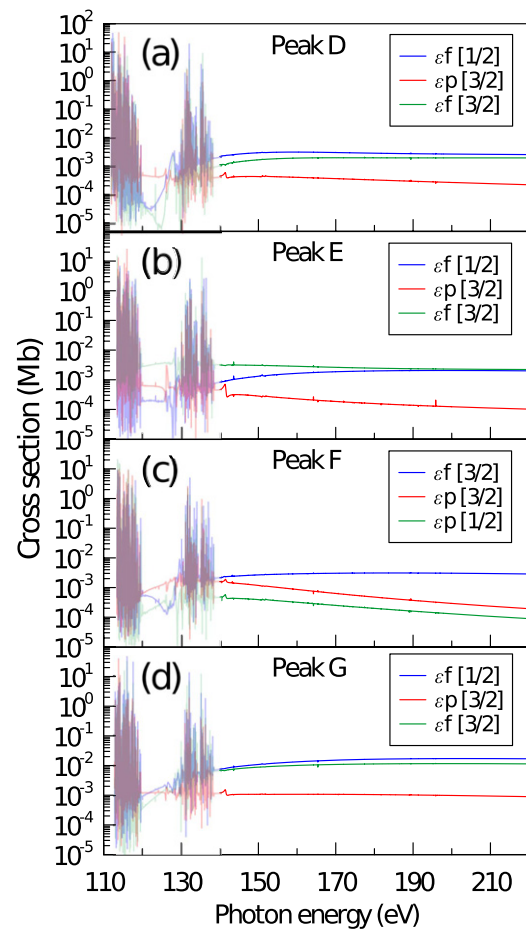


Figure 11. Photoionization partial cross sections for peak D (a), peak E (b), peak F (c) and peak G (d). For the sake of clarity, the theoretical results in the autoionization regions are plotted more lightly.

sections corresponding to peak H (figure 12(a)) show that the dominant contribution is due to the d-waves, which could arise from either a normal or a conjugate shake-up mechanism, or to a strong interference between both formation mechanisms. An interesting point in regard to peak H is that this is the only peak in the binding energy range of 110–118 eV with the normal shake-up mechanism corresponding to the process of dipole ionization from the 4p orbital together with monopole excitation from the 3d orbital.

For peaks I (figure 12(b)), K (figure 13(a)) and L (figure 13(b)), all the quantum numbers are the same as those for peak D. Therefore, these peaks are formed through a normal shake-up mechanism. For peaks J (figure 12(c)) and M (figure 13(c)), all the quantum numbers are the same as those for peak F. Thus, the normal shake-up process is the dominant formation mechanism.

4.4. The $Kr^+ 3d^{-1}4s^{-1}nl$ correlation satellites

In our experimental spectra recorded at photon energies of 190 and 200 eV, the upper limit of the binding energy range was extended to 132 eV to enable the peaks associated with the $3d^{-1}4s^{-1}nl$ ($l = s, p, d$) correlation satellites to be observed. These satellites occur in the binding energy range

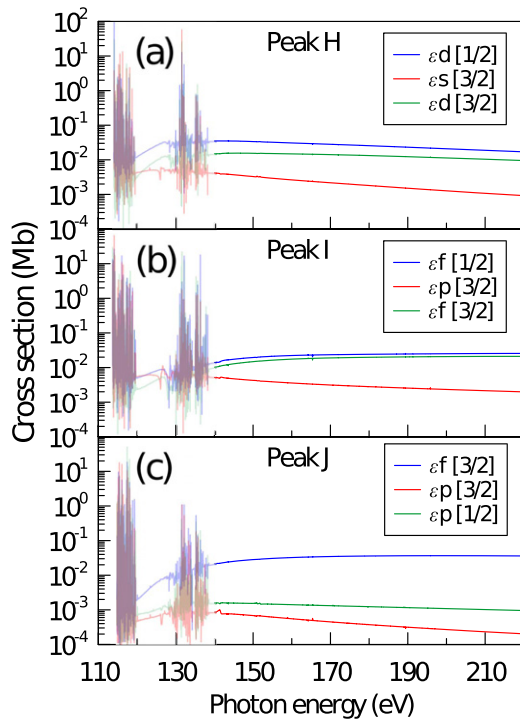


Figure 12. Photoionization partial cross sections for peak H (a), peak I (b) and peak J (c). For the sake of clarity, the theoretical results in the autoionization regions are plotted more lightly.

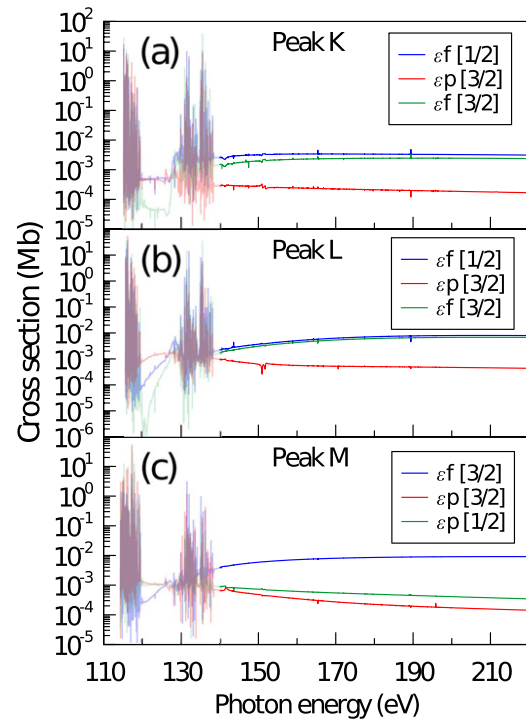


Figure 13. Photoionization partial cross sections for peak K (a), peak L (b) and peak M (c). For the sake of clarity, the theoretical results in the autoionization regions are plotted more lightly.

~124–132 eV. In the polarization dependent spectra plotted in figure 8, it is noticeable that the peak intensities in the $\theta = 0^\circ$ spectrum are approximately the same as those in the $\theta = 90^\circ$ spectrum, indicating that at $h\nu = 190$ eV the β -values for the peaks associated with the $3d^{-1}4s^{-1}nl$ states are approximately zero. The peak intensity distribution changes very little in the spectrum recorded at $h\nu = 200$ eV, although at this photon energy the β -values of all the peaks are very slightly greater than zero.

The results from our R-matrix calculations, and the experimental magic angle spectrum recorded at $h\nu = 190$ eV, are plotted in figure 14. The identification of the peaks, in terms of the leading configuration, are given in table 4. The peaks have been labelled and numbered according to their binding energy range. In general, the simulated spectrum reproduces the main features observed in the experimental spectrum. If only the leading configuration (table 4) for the $3d^9 4s^1 4p^6 nl$ correlation satellites is considered, then very few of the peaks can be attributed to dipole ionization of the 3d orbital accompanied by monopole excitation of the 4s orbital (process *SU2*). Many of the peaks can only be formed through process *SU4*, dipole ionization of the 4s electron accompanied by monopole excitation of the 3d electron.

We consider the peaks comprising the W_1 , W_2 and W_3 groups in greater detail. Peaks $W_1^{(1)}-W_3^{(7)}$ are formed through shake-up process *SU4*, but for peak $W_3^{(8)}$ a more interesting situation occurs. The l -dependent photoionization partial cross sections for peak $W_3^{(8)}$ are plotted in figure 15 and it is evident that the p-wave, which should be the sole contribution for mechanism *SU4*, dominates only in the photon energy

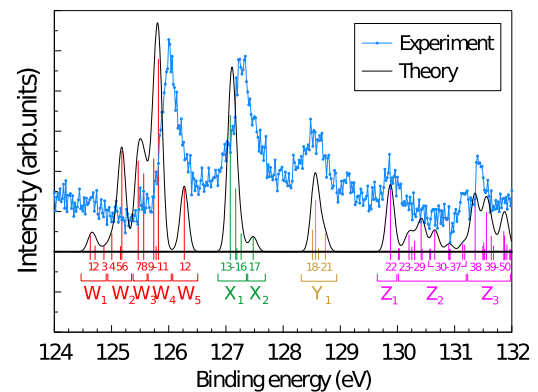


Figure 14. The magic angle photoelectron spectrum obtained from the polarization dependent spectra recorded at a photon energy of 190 eV, together with the simulated spectrum, in the binding energy region corresponding to $3d^{-1}4s^{-1}nl$ states. All the labels on the plot correspond to those given in table 4. The thick black horizontal line corresponds to the zero intensity.

range 140–160 eV. Starting from ~160 eV, the contributions from the $\varepsilon p [3/2]$ and $\varepsilon f [1/2]$ waves become approximately equal, but for energies above 180 eV the $\varepsilon f [1/2]$ wave constitutes the largest contribution. Such a behaviour is inconsistent with mechanism *SU4* because f-waves are not allowed. Peak $W_3^{(8)}$, having a configuration $3d^9 4s^1 4p^6 (^1D) 4d [^2D_{5/2}]$ with a leading percentage of 66%, has substantial admixtures of the $3d^9 4s^1 4p^6 (^3D) 5s [^2D_{5/2}]$ (4.5%) and $3d^9 4s^1 4p^6 (^1D) 5s [^2D_{5/2}]$ (2.5%) configurations. The $3d^9 4s^1 4p^6 5s$ configurations may be produced through the normal shake-up process *SU2* with the creation of p- and f-waves. Thus, this additional shake-up

Table 4. Identification of the photoelectron peaks appearing in the simulated spectra encompassing the $\text{Kr}^+ 3d^9 4s^1 4p^6 nl$ correlation satellites. The leading electron configuration and the term is given for each peak. The first parenthesis indicates the $3d^9 4s$ electronic state, and the total term of the electron configuration with total momentum J is given in square brackets.

Peak label	Identification	Leading percentages
W ₁	W ₁ ⁽¹⁾ 3d ⁹ 4s ¹ 4p ⁶ (³ D)4d[² P _{1/2}]	50%
	W ₁ ⁽²⁾ 3d ⁹ 4s ¹ 4p ⁶ (³ D)4d[² P _{3/2}]	46%
	W ₁ ⁽³⁾ 3d ⁹ 4s ¹ 4p ⁶ (¹ D)4d[² F _{5/2}]	50%
W ₂	W ₂ ⁽⁴⁾ 3d ⁹ 4s ¹ 4p ⁶ (³ D)4d[² D _{3/2}]	45%
	W ₂ ⁽⁵⁾ 3d ⁹ 4s ¹ 4p ⁶ (³ D)4d[² D _{5/2}]	72%
	W ₂ ⁽⁶⁾ 3d ⁹ 4s ¹ 4p ⁶ (¹ D)4d[² S _{1/2}]	46%
W ₃	W ₃ ⁽⁷⁾ 3d ⁹ 4s ¹ 4p ⁶ (¹ D)4d[² P _{3/2}]	58%
	W ₃ ⁽⁸⁾ 3d ⁹ 4s ¹ 4p ⁶ (¹ D)4d[² D _{5/2}]	66%
W ₄	W ₄ ⁽⁹⁾ 3d ⁹ 4s ¹ 4p ⁶ (³ D)5p[² P _{3/2}]	85%
	W ₄ ⁽¹⁰⁾ 3d ⁹ 4s ¹ 4p ⁶ (³ D)5p[² D _{5/2}]	90%
	W ₄ ⁽¹¹⁾ 3d ⁹ 4s ¹ 4p ⁶ (³ D)5s[² D _{5/2}]	61%
W ₅	W ₅ ⁽¹²⁾ 3d ⁹ 4s ¹ 4p ⁶ (¹ D)4d[² P _{1/2}]	45%
X ₁	X ₁ ⁽¹³⁾ 3d ⁹ 4s ¹ 4p ⁶ (³ D)5s[² D _{3/2}]	72%
	X ₁ ⁽¹⁴⁾ 3d ⁹ 4s ¹ 4p ⁶ (³ D)5p[² P _{1/2}]	90%
	X ₁ ⁽¹⁵⁾ 3d ⁹ 4s ¹ 4p ⁶ (³ D)5p[² F _{5/2}]	48%
	X ₁ ⁽¹⁶⁾ 3d ⁹ 4s ¹ 4p ⁶ (¹ D)5p[² D _{3/2}]	46%
X ₂	X ₂ ⁽¹⁷⁾ 3d ⁹ 4s ¹ 4p ⁶ (³ D)4d[² S _{1/2}]	56%
Y ₁	Y ₁ ⁽¹⁸⁾ 3d ⁹ 4s ¹ 4p ⁶ (¹ D)5p[² P _{3/2}]	85%
	Y ₁ ⁽¹⁹⁾ 3d ⁹ 4s ¹ 4p ⁶ (¹ D)4d[² D _{3/2}]	48%
	Y ₁ ⁽²⁰⁾ 3d ⁹ 4s ¹ 4p ⁶ (¹ D)5p[² D _{5/2}]	88%
	Y ₁ ⁽²¹⁾ 3d ⁹ 4s ¹ 4p ⁶ (³ D)4d[² F _{5/2}]	50%
Z ₁	Z ₁ ⁽²²⁾ 3d ⁹ 4s ¹ 4p ⁶ (³ D)6s[² D _{5/2}]	98%
Z ₂	Z ₂ ⁽²³⁾ 3d ⁹ 4s ¹ 4p ⁶ (¹ D)6s[² D _{3/2}]	53%
	Z ₂ ⁽²⁴⁾ 3d ⁹ 4s ¹ 4p ⁶ (³ D)5d[² P _{3/2}]	71%
	Z ₂ ⁽²⁵⁾ 3d ⁹ 4s ¹ 4p ⁶ (³ D)5d[² D _{5/2}]	76%
	Z ₂ ⁽²⁶⁾ 3d ⁹ 4s ¹ 4p ⁶ (³ D)5d[² P _{1/2}]	64%
	Z ₂ ⁽²⁷⁾ 3d ⁹ 4s ¹ 4p ⁶ (³ D)6p[² P _{3/2}]	85%
	Z ₂ ⁽²⁸⁾ 3d ⁹ 4s ¹ 4p ⁶ (³ D)6p[² D _{5/2}]	88%
	Z ₂ ⁽²⁹⁾ 3d ⁹ 4s ¹ 4p ⁶ (³ D)5d[² D _{3/2}]	38%
	Z ₂ ⁽³⁰⁾ 3d ⁹ 4s ¹ 4p ⁶ (¹ D)5d[² F _{5/2}]	41%
	Z ₂ ⁽³¹⁾ 3d ⁹ 4s ¹ 4p ⁶ (¹ D)6s[² D _{5/2}]	98%
	Z ₂ ⁽³²⁾ 3d ⁹ 4s ¹ 4p ⁶ (¹ D)5d[² P _{1/2}]	72%
	Z ₂ ⁽³³⁾ 3d ⁹ 4s ¹ 4p ⁶ (³ D)6p[² F _{5/2}]	52%
	Z ₂ ⁽³⁴⁾ 3d ⁹ 4s ¹ 4p ⁶ (³ D)6p[² P _{1/2}]	55%
	Z ₂ ⁽³⁵⁾ 3d ⁹ 4s ¹ 4p ⁶ (³ D)6p[² D _{3/2}]	50%
	Z ₂ ⁽³⁶⁾ 3d ⁹ 4s ¹ 4p ⁶ (¹ D)5d[² P _{3/2}]	64%
	Z ₂ ⁽³⁷⁾ 3d ⁹ 4s ¹ 4p ⁶ (¹ D)5d[² D _{5/2}]	77%

(continued on next page)

Table 4. Continued

Peak label	Identification	Leading percentages
$Z_3^{(38)}$	$3d^9 4s^1 4p^6(^3D)6s[{}^2D_{3/2}]$	53%
$Z_3^{(39)}$	$3d^9 4s^1 4p^6(^1D)6p[{}^2P_{3/2}]$	85%
$Z_3^{(40)}$	$3d^9 4s^1 4p^6(^1D)5d[{}^2S_{1/2}]$	48%
$Z_3^{(41)}$	$3d^9 4s^1 4p^6(^1D)6p[{}^2D_{5/2}]$	87%
$Z_3^{(42)}$	$3d^9 4s^1 4p^6(^3D)7s[{}^2D_{5/2}]$	94%
$Z_3^{(43)}$	$3d^9 4s^1 4p^6(^1D)5d[{}^2D_{3/2}]$	35%
$Z_3^{(44)}$	$3d^9 4s^1 4p^6(^3D)5d[{}^2F_{5/2}]$	41%
$Z_3^{(45)}$	$3d^9 4s^1 4p^6(^3D)7p[{}^2P_{3/2}]$	81%
$Z_3^{(46)}$	$3d^9 4s^1 4p^6(^1D)6p[{}^2P_{1/2}]$	55%
$Z_3^{(47)}$	$3d^9 4s^1 4p^6(^3D)7p[{}^2D_{5/2}]$	69%
$Z_3^{(48)}$	$3d^9 4s^1 4p^6(^1D)6p[{}^2F_{5/2}]$	37%
$Z_3^{(49)}$	$3d^9 4s^1 4p^6(^1D)6p[{}^2D_{3/2}]$	49%
$Z_3^{(50)}$	$3d^9 4s^1 4p^6(^3D)7s[{}^2D_{3/2}]$	52%

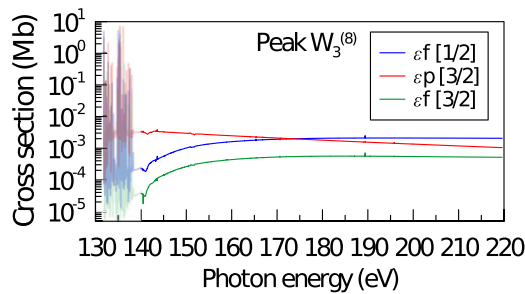


Figure 15. Photoionization partial cross sections for peak $W_3^{(8)}$ from the W_3 -group (table 4). For the sake of clarity, the theoretical results in the autoionization regions are plotted more lightly.

mechanism explains the predicted f-wave component for peak $W_3^{(8)}$.

5. Summary

We have studied the Kr 3d correlation satellites and main lines, both experimentally and theoretically, concentrating on the photoelectron intensities and angular distributions, and the photoionization cross sections. Such experimental studies have become possible with the advent of the new generation of synchrotron radiation sources, giving a new impetus to the development of atomic inner shell photoelectron spectroscopy. We have performed extensive R-matrix calculations of the total and partial Kr 3d photoionization cross sections in the photon energy region 80–230 eV, simulated PES, and evaluated the anisotropy parameters for both the main lines and the correlation satellites. Spin–orbit splitting is taken into account in our calculations. Our simulated PES, and our calculated anisotropy parameters, show qualitative agreement with the experimental results. Quantitatively, the agreement between the measured and the simulated PES is good in the binding energy region 108–115 eV, and is reasonable in the range 115–118 eV. For most of the photoelectron peaks, the calculated anisotropy parameters are very close to the experimental

values, at least in the resonance-free region (i.e. >140 eV). Our calculations allow the satellites arising from the $3d^{-1}4p^{-1}nl$ and $3d^{-1}4s^{-1}nl$ configurations to be identified. For the peaks observed in the binding energy region 110–118 eV, our calculations allow the satellite formation mechanisms, in terms of normal and conjugate shake-up processes, to be defined. In most cases the PAD measurements confirm the predicted mechanisms. However, in many cases, the identification of the satellites based on simple phenomenological arguments of the photon energy dependent behaviour of their branching ratios or betas is not a fruitful approach, since the computational work reveals complex interplay between contributing channels with possible interference.

The main theoretical limitation to the present work is associated with the available computational powers, which restrict the number of ionic (threshold) electronic configurations. Although all the thresholds corresponding to direct photoionization in the considered range of photon energies were included in the calculations, there is, however, a fairly large number of states with excitations that were not taken into account in this work (especially those arising from configurations with nf -electron). As some of the shake-up states with the configuration $3d^{-1}4p^{-1}nl$ are energetically very close to each other and have quite high configuration mixing coefficients, additional channel interference effects can be expected if these higher excited states were included in the calculations. Therefore, a better agreement between experiment and theory for the shape of the photoelectron spectrum, together with the addition of lines that were not found in the present model (in the binding energy range 118–122 eV), would be anticipated.

The main experimental limitation to the present work is associated with the overlap between the peaks arising from the Auger decay of a $(3d)^{-1}$ hole state and those due to the 3d correlation satellites. In principle, this difficulty could be overcome by electron–electron coincidence measurements involving the initial 3d photoelectron and the subsequent Auger electron. The resulting spectrum, due purely to Auger transitions, could then be subtracted from the non-coincident spectrum, containing contributions from both photoelectrons and

Auger electrons, to obtain a spectrum due only to photoelectrons. Such a procedure, performed at a series of photon energies, would allow the correlation satellites to be studied free from contaminating Auger structure. However, such coincidence measurements would require either a magnetic bottle spectrometer, where the inherent low energy resolution would limit the observable structure, or two hemispherical analysers, where the coincidence count rate would be prohibitively low.

Acknowledgments

DMPH is grateful to the Science and Technology Facilities Council (United Kingdom) for financial support. The research leading to this result has been supported by the Project CALIPSOplus under the Grant Agreement 730872 from the EU Framework Programme for Research and Innovation HORIZON 2020. ANG-G and MDK acknowledge funding by the Russian Foundation for Basic Research (RFBR) under the research Project No. 20-52-12023 and support from Russian Ministry of Science and Education Grant No. 075-15-2021-1353. The work of MDK is also supported by the Ministry of Science and Higher Education of the Russian Federation (Project No. 0818-2020-0005) using resources of the Shared Services Center 'Data Center of the Far-Eastern Branch of the Russian Academy of Sciences'. MP and MR acknowledge Academy of Finland. We acknowledge MAX IV Laboratory for time on Beamline FinEstBeAMS under Proposal 20180394. Research conducted at MAX IV, a Swedish national user facility, is supported by the Swedish Research council under Contract 2018-07152, the Swedish Governmental Agency for Innovation Systems under Contract 2018-04969, and Formas under Contract 2019-02496.

Data availability statement

The data that support the findings of this study are available upon reasonable request from the authors.

ORCID iDs

M D Kiselev  <https://orcid.org/0000-0003-1658-6192>
 M Reinhardt  <https://orcid.org/0000-0002-3396-0679>
 M Patanen  <https://orcid.org/0000-0002-2970-7494>
 A Kivimäki  <https://orcid.org/0000-0003-0753-8164>
 I Powis  <https://orcid.org/0000-0002-7941-9079>
 A N Grum-Grzhimailo  <https://orcid.org/0000-0003-1415-7327>
 D M P Holland  <https://orcid.org/0000-0003-1351-605X>

References

- [1] Carlson T A 1967 *Phys. Rev.* **156** 142
- [2] Gelius U 1974 *J. Electron Spectrosc. Relat. Phenom.* **5** 985
- [3] Wuilleumier F and Krause M O 1974 *Phys. Rev. A* **10** 242
- [4] Siegbahn H and Karlsson L 1982 *Encyclopedia of Physics* vol 31 ed W Mehlhorn (Berlin: Springer) p 215
- [5] Svensson S, Eriksson B, Mårtensson N, Wendin G and Gelius U 1988 *J. Electron Spectrosc. Relat. Phenom.* **47** 327
- [6] Åberg T 1967 *Phys. Rev.* **156** 35
- [7] Carlson T A, Nestor C W, Tucker T C and Malik F B 1968 *Phys. Rev.* **169** 27
- [8] Martin R L and Shirley D A 1977 *Electron Spectroscopy: Theory, Techniques and Applications* vol 1 ed C R Brundle and A D Baker (London: Academic) p 76
- [9] Becker U and Shirley D A 1990 *Phys. Scr.* **T31** 56
- [10] Schmidt V 1992 *Rep. Prog. Phys.* **55** 1483
- [11] Krause M O, Whitfield S B, Caldwell C D, Wu J-Z, van der Meulen P, de Lange C A and Hansen R W C 1992 *J. Electron Spectrosc. Relat. Phenom.* **58** 79
- [12] Kikas A, Osborne S J, Ausmees A, Svensson S, Sairanen O-P and Aksela S 1996 *J. Electron Spectrosc. Relat. Phenom.* **77** 241
- [13] Travnikova O et al 2019 *J. Phys. Chem. A* **123** 7619
- [14] Schiff L I 1968 *Quantum Mechanics* (New York: McGraw-Hill)
- [15] Thomas T D 1984 *Phys. Rev. Lett.* **52** 417
- [16] Berkowitz J, Dehmer J L, Kim Y K and Desclaux J P 1974 *J. Chem. Phys.* **61** 2556
- [17] Langer B, Viehhaus J, Hemmers O, Menzel A, Wehlitz R and Becker U 1991 *Phys. Rev. A* **43** 1652
- [18] Hemmers O, Whitfield S B, Berrah N, Langer B, Wehlitz R and Becker U 1995 *J. Phys. B: At. Mol. Opt. Phys.* **28** L693
- [19] Kempgens B, Kivimäki A, Köppe H M, Neeb M, Bradshaw A M and Feldhaus J 1997 *J. Chem. Phys.* **107** 4219
- [20] Adam M Y, Morin P and Wendin G 1985 *Phys. Rev. A* **31** 1426
- [21] Heimann P A, Becker U, Kerckhoff H G, Langer B, Szostak D, Wehlitz R, Lindle D W, Ferrett T A and Shirley D A 1986 *Phys. Rev. A* **34** 3782
- [22] Kossmann H, Krässig B, Schmidt V and Hansen J E 1987 *Phys. Rev. Lett.* **58** 1620
- [23] Becker U et al 1988 *Phys. Rev. Lett.* **60** 1490
- [24] Langer B, Viehhaus J, Hemmers O, Menzel A, Wehlitz R and Becker U 1995 *Phys. Rev. A* **51** R882
- [25] Berrah N et al 1997 *Phys. Rev. A* **56** 4545
- [26] Lagutin B M et al 1996 *J. Phys. B: At. Mol. Opt. Phys.* **29** 937
- [27] Slattery A E, Wightman J P, MacDonald M A, Cvejanović S and Reddish T J 2000 *J. Phys. B: At. Mol. Opt. Phys.* **33** 4833
- [28] Yoshii H, Aoto T, Morioka Y and Hayaishi T 2007 *J. Phys. B: At. Mol. Opt. Phys.* **40** 2765
- [29] Bristow D J, Tse J S and Bancroft G M 1982 *Phys. Rev. A* **25** 1
- [30] Lindle D W, Heimann P A, Ferrett T A, Kobrin P H, Truesdale C M, Becker U, Kerckhoff H G and Shirley D A 1986 *Phys. Rev. A* **33** 319
- [31] Sankari R, Kivimäki A, Aksela H, Aksela S, Prince K C, Coreno M, Alagia M and de Simone M 2003 *Phys. Rev. A* **67** 032710
- [32] Hayaishi T, Murakami E, Morioka Y, Aksela H, Aksela S, Shigemasa E and Yagishita A 1991 *Phys. Rev. A* **44** R2771
- [33] Bolognesi P, Avaldi L, Lopes M C A, Dawber G, King G C, MacDonald M A, Villani C and Tarantelli F 2001 *Phys. Rev. A* **64** 012701
- [34] Pärna R et al 2017 *Nucl. Instrum. Methods Phys. Res. A* **859** 83
- [35] Chernenko K et al 2021 *J. Synchrotron Radiat.* **28** 1620
- [36] Kooser K, Kivimäki A, Turunen P, Pärna R, Reisberg L, Kirm M, Valden M, Huttula M and Kukk E 2020 *J. Synchrotron Radiat.* **27** 1080
- [37] Patanen M et al 2021 *J. Chem. Phys.* **155** 054304
- [38] Sasaki S, Kakuno K, Takada T, Shimada T, Yanagida K and Miyahara Y 1993 *Nucl. Instrum. Methods Phys. Res. A* **331** 763
- [39] Follath R and Senf F 1997 *Nucl. Instrum. Methods Phys. Res. A* **390** 388
- [40] Baltzer P, Karlsson L, Lundqvist M and Wannberg B 1993 *Rev. Sci. Instrum.* **64** 2179
- [41] Cooper J and Zare R N 1968 *J. Chem. Phys.* **48** 942

- [42] Powis I et al 2015 *J. Chem. Phys.* **143** 144304
- [43] Holland D M P, Nandi S, Nicolas C, Bozek J D, Patanen M and Powis I 2021 *Chem. Phys.* **542** 111050
- [44] Southworth S H, Parr A C, Hardis J E, Dehmer J L and Holland D M P 1986 *Nucl. Instrum. Methods Phys. Res. A* **246** 782
- [45] Houlgate R G, Codling K, Marr G V and West J B 1974 *J. Phys. B: At. Mol. Phys.* **7** L470
- [46] Aksela H, Aksela S and Pulkkinen H 1984 *Phys. Rev. A* **30** 2456
- [47] Jauhiainen J, Aksela H, Aksela S, Kivimäki A, Sairanen O-P, Nömmiste E and Végh J 1995 *J. Phys. B: At. Mol. Opt. Phys.* **28** 3831
- [48] Partanen L, Huttula M, Aksela H and Aksela S 2007 *J. Phys. B: At. Mol. Opt. Phys.* **40** 3795
- [49] Zatsarinny O 2006 *Comput. Phys. Commun.* **174** 273
- [50] Fischer C F, Brage T and Jonsson P 1997 *Computational Atomic Structure: An MCHF Approach* (Bristol: Institute of Physics Publishing)
- [51] Racah G 1942 *Phys. Rev.* **61** 537
- [52] Marr G V and West J B 1976 *At. Data Nucl. Data Tables* **18** 497
- [53] Tulkki J, Aksela S, Aksela H, Shigemasa E, Yagishita A and Furusawa Y 1992 *Phys. Rev. A* **45** 4640
- [54] Chan W F, Cooper G, Guo X, Burton G R and Brion C E 1992 *Phys. Rev. A* **46** 149
- [55] Kennedy D J and Manson S T 1972 *Phys. Rev. A* **5** 227
- [56] Shanthi N, Deshmukh P C and Manson S T 1988 *Phys. Rev. A* **37** 4720
- [57] Cooper J W and Manson S T 1969 *Phys. Rev.* **177** 157